Electrical Double Layers Modulate the Growth of Solid-Electrolyte Interphases

Jaehyeon Kim[1,2], Fujia Zhao[1,2], Lalith Krishna Samanth Bonagiri[2,3], Qian Ai[1,2], and Yingjie Zhang[1,2,4]*

1. Department of Materials Science and Engineering, University of Illinois, Urbana, Illinois 61801, United States

2. Materials Research Laboratory, University of Illinois, Urbana, Illinois 61801, United States

3. Department of Mechanical Science and Engineering, University of Illinois, Urbana, Illinois 61801, United States

4. Beckman Institute for Advanced Science and Technology, University of Illinois, Urbana, Illinois 61801, United States

*Correspondence to: yjz@illinois.edu

Abstract: Solid-electrolyte interphases (SEIs), oftentimes viewed as the most important yet least understood part of alkali ion/metal batteries, remain a key bottleneck for battery design. Despite extensive research in the past few decades, to date we have only begun to unravel the structure of SEIs, while its dynamic nucleation and growth mechanism is still elusive. Here we discuss the existing progress in characterizing SEIs in the battery community, and propose that SEI growth depends critically on the electrical double layer (EDL) structure, a factor that has been largely hidden or ignored to date. We will further discuss methods for simultaneously characterizing EDL and SEIs, with a particular focus on the emerging electrochemical 3D atomic force microscopy (EC-3D-AFM) and shell-isolated nanoparticle-enhanced Raman spectroscopy (SHINERS) techniques. In the end, we will propose strategies for predictive design of electrolytes to enable controlled EDL and SEI structures and achieve desired battery performance.

Introduction

In electrochemical systems, the key energy conversion events occur at the electrode-electrolyte interfaces.[1,2] For alkali ion and alkali metal batteries, SEIs grown at anode-electrolyte interfaces have been widely known as one of the "most important yet least understood" components.[2–6] SEIs allow ionic conduction while blocking electronic transport, thus preventing extensive redox reactions of the electrolyte species, enabling a high voltage output of the battery. To characterize the composition and structure of SEIs, the past decade has seen strong efforts from many research groups worldwide in imaging (electron and scanning probe microscopy),[7–14] spectroscopy (vibrational, X-ray, mass spectrometry, etc.),[6,15–18] and diffraction/reflectometry (neutron and X-ray) measurements,[19–21] either in situ or ex situ. While the precise structure of SEIs is still under debate, the overall SEI morphology and composition are being gradually unfolded.

Here we mainly focus on the widely used lithium-ion batteries (LIBs). Traditional electrolytes for LIBs consist of ~1 M $LiPF_6$ salt in mixture solvents comprised of ethylene carbonate (EC), linear carbonate esters (dimethyl carbonate (DMC), diethyl carbonate (DEC), ethyl methyl carbonate (EMC), etc.), and additives (e.g. fluoroethylene carbonate (FEC) and vinylene carbonate (VC)).[2,8,10–13,16–20,22] Existing studies on LIBs have revealed multi-component SEI structures that contain both inorganic compounds such as LiF, Li_2O, and Li_2CO_3, and organic species such as lithium alkyl carbonates.[2,8,10–13,16–20,22]

In contrast to the tremendous efforts on probing the SEI structure, its dynamic formation mechanism has rarely been studied. Specifically, how do the SEI growth process and eventual structure depend on the electrolyte composition and concentration, and how can we rationally design the electrolytes to achieve the desirable SEIs? Such questions are becoming increasingly pressing, as various new types of electrolytes are being actively developed with the goal of increasing the stability and energy density of LIBs. Examples include: organic electrolytes with different/multiple additives,[21,23] ionic liquids,[24] aqueous solutions,[25] and various highly concentrated electrolytes.[6,11,26–30] Remarkably, it has been observed that "slight" modifications to the electrolyte, such as the addition of small amounts of organic additives and the increase of salt concentration, have significant impacts on the SEI composition.[2,6,11,23,26–30]

To explain the sensitive dependence of SEI on the electrolyte composition, it was proposed that the Li^+ solvation shell in the bulk electrolyte solution provides the source of molecules that are reduced at the electrode surface forming SEI.[31,32] This hypothesis has been partially supported by experimental studies that reveal some correlation between bulk Li^+ solvation structure and the SEI composition.[32–34] However, this correlation by itself is far from sufficient in explaining and predicting the complex overall SEI structure. In recent years, it has been increasingly clear that a comprehensive description of the SEI formation process requires explicit knowledge of the EDL structure, which provides the direct source for electroreduction and the subsequent nucleation and growth of SEI.[6,35–38] For example, simulations have predicted that the Li^+ coordination configuration at charged EDLs is distinct from that of the bulk electrolyte, resulting in up to 1–2 eV changes in the reduction potential of solvent and anion species, thus significantly modulating the reduction probability of these species.[35] In addition, the free solvent molecules and salt anions in the EDL (if present), likely with different ratio from that of the bulk liquid, may also be electrochemically reduced and contribute to the later stage of SEI growth, which further complicates the overall process. Therefore, without a thorough comprehension of the EDL structure under realistic battery operating conditions, the exact SEI growth mechanism will remain a puzzle.

Despite the urgent demand in understanding EDLs, their experimental characterization has been highly challenging, due to the delicate, fluidic, and buried nature of such interfacial structures. To date only a handful of tools have demonstrated capabilities in probing the EDL structure, mainly including X-ray scattering (XRS),[39,40] vibrational and X-ray spectroscopies,[41–47] and scanning probe microscopy,[48–57] providing information on the crystallographic structure, chemical composition/bonding states, and local morphology/density distribution, respectively. Each of these methods has unique advantages and limitations; when used alone, it is oftentimes insufficient to determine the full molecular details of the EDL structure. At the battery anodes, the heterogeneity of SEIs further complicates the overall interfacial structure. Therefore, a thorough investigation of the EDL, SEI, and their correlations will inevitably require the synergistic combination of multiple methods, which has rarely been achieved to date.

In this perspective, we first discuss two particularly promising methods that may enable the simultaneous characterization of EDL and SEI: EC-3D-AFM (electrochemical 3D atomic force microscopy) and SHINERS (shell-isolated nanoparticle-enhanced Raman spectroscopy). We will then propose future research directions where these two methods are combined to study the in situ EDL evolution and SEI growth dynamics. Eventually, we will discuss the implications of the EDL-SEI correlation on the rational and predictive design of LIBs.

EC-3D-AFM Characterization

EC-3D-AFM is essentially a combination of two methods, EC-AFM and 3D-AFM (Figure 1). Here we will discuss the developments and current progress in each of these techniques, and how their combination, as realized in our lab, enables new opportunities in imaging heterogeneous electrode-electrolyte interfaces including EDLs and SEIs.

EC-AFM was first demonstrated in the 1990s.[58–61] The early work used contact mode to image the electrode surface immersed in electrolyte (Figure 1a), and observed nucleation and growth processes in situ. Although atomic scale lattice images were reported in certain cases, later on it was realized that the contact mode images can rarely achieve "true atomic resolution" due to the large probe-sample contact area.[62–64] In addition, the high probe-sample contact forces also tend to displace species that are not strongly bound or adsorbed on the electrode surface. These limitations triggered the development of AC mode (amplitude modulation or frequency modulation) EC-AFM beginning from the late 1990s.[65–69] Using these intermittent contact or non-contact modes, perturbations to the electrode surface is much weaker. Also, since the AC response (amplitude, phase, and/or frequency shift) is inherently sensitive to the tip-sample force gradient, instead of the total force sensed by the DC mode, the ultimate resolution of the AC mode can be much higher.[70] However, the typically used piezoacoustic excitation (for inducing probe oscillation), while sufficient for imaging in air, results in large mechanical noise and "a forest of peaks" in the frequency response of the cantilever.[71–73] This is because the acoustic excitation generates mechanical oscillation of the whole AFM probe holder, which couples to the hydrodynamic motion of the liquid, leading to large noise. To avoid these noise problems that would occur near resonance frequency, the past decade has seen tremendous progress in developing and using peak force tapping (PFT), which modulates the z motion of the probe at lower frequency (100–1000 Hz) and images the sample via intermittent contact modes.[74] As an "intermediate regime" between contact and AC mode AFM, PFT has found broad applications in imaging SEIs at battery anodes, due to their ease of use and weak perturbative nature.[36,75–78] Nevertheless, PFT still suffers from similar resolution limits as contact mode AFM, since both are based on DC cantilever deflection measurements that limit the resolution to the probe radius (a few nanometers in best cases).

To enable reliable, high-resolution imaging in liquid, AC mode is still desirable, yet the "forest of peaks" problem must be solved. Fortunately, a truly remarkable invention, photothermal excitation, solved this exact problem (Figure 1b). Developed in the late 2000s and early 2010s,[73,79–83] photothermal excitation replaces the piezoacoustic drive, and triggers the cantilever resonance via an intensity-modulated laser through periodic photo-induced thermal expansion and contraction of the cantilever. Due to the localization of the excitation spot (typically near the end of the microlever beam), the mechanical oscillation only occurs in the microlever, while the much larger microchip body (support of the cantilever) and other parts of the probe holder remain mostly static. Therefore, the background oscillations are largely removed and smooth cantilever resonance can be reliably excited, enabling true atomic resolution imaging in liquid.[81,82]

Equipped with the photothermal excitation method, 3D-AFM was developed to image not only the atomic structure of the solid surface, but also the surrounding EDLs.[48–54,84–86] 3D motion of the probe was achieved by driving the z scan via a sinusoidal wave, and the x, y scan in linear patterns. Throughout 2010s, 3D-AFM was almost exclusively used to image the EDL of aqueous solutions

in a droplet configuration (Figure 1b),[49–54,84,86] where the water droplet was exposed to air and stabilized via surface tension between the probe holder and the solid substrate. This simple design avoids the usage of liquid containers with side walls, thus minimizing any possible excess contamination and extra noise during the tip/sample scanning process. However, the small droplet (e.g., 20–50 μL in volume) tends to evaporate quickly (within one to a few hours) and the open configuration is susceptible to airborne contaminations that may diffuse into the droplet over time.[87] In addition, for applications in electrochemical systems, such simplified configuration makes it challenging to insert reference and counter electrodes into the small droplet and achieve controlled electrochemical potential and environment.

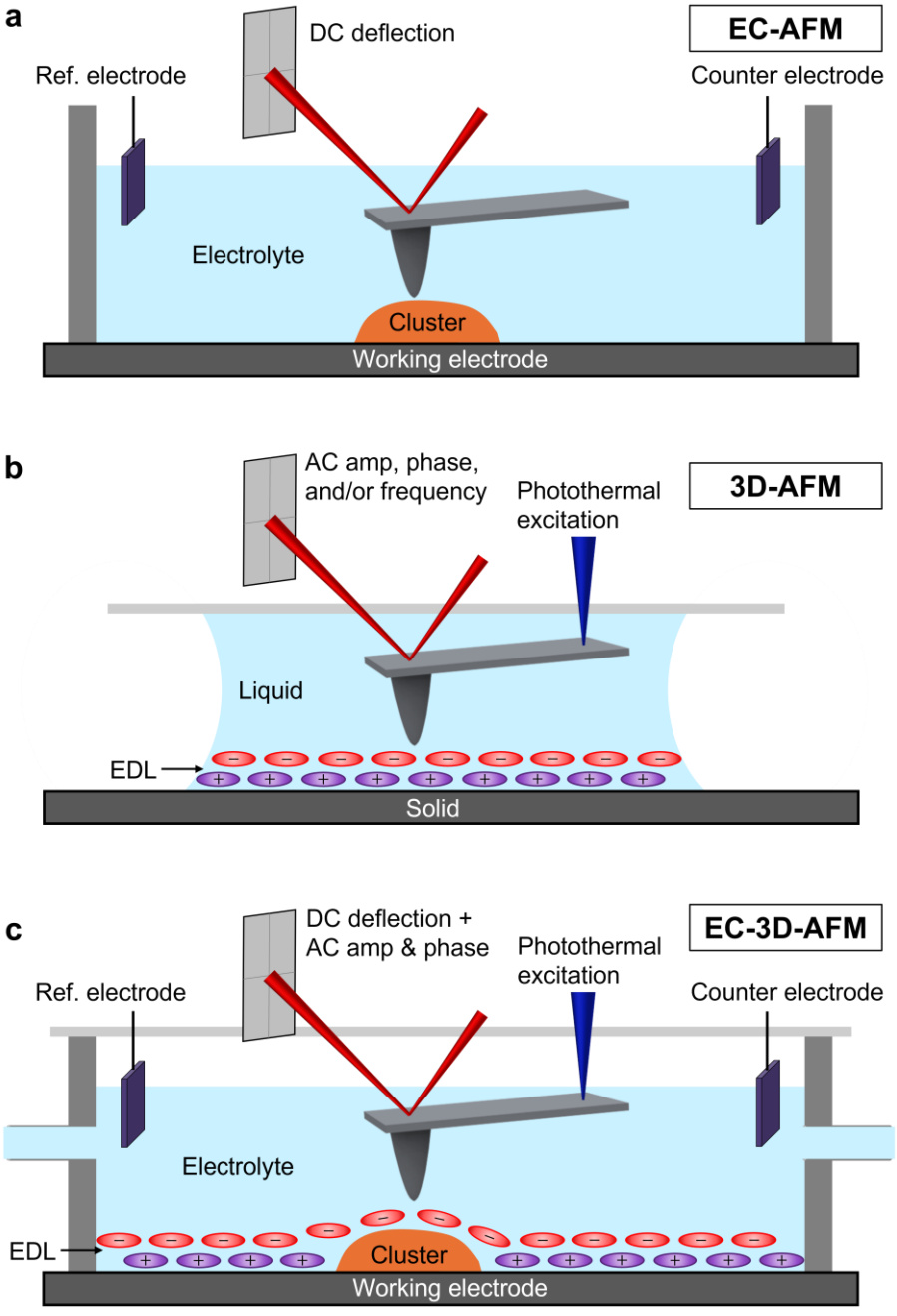

Figure 1. Schematics of (**a**) EC-AFM, (**b**) 3D-AFM, and (**c**) EC-3D-AFM methods.

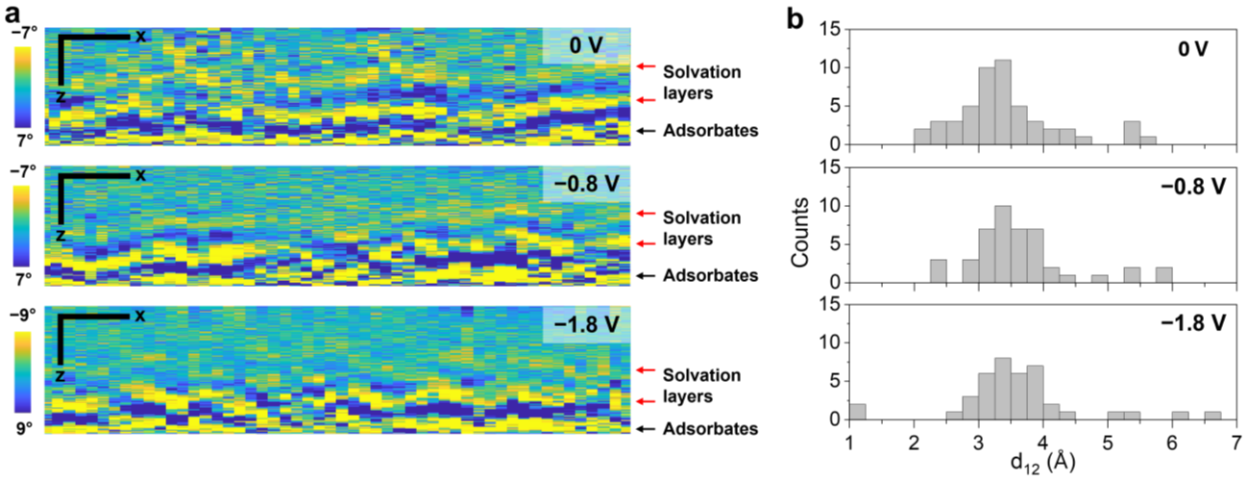

Figure 2. EC-3D-AFM imaging at heterogeneous electrode sites. (**a**) EC-3D-AFM (x-z cross section) phase maps of the EDL of 0.1 M K_2SO_4 solution in water on adventitious molecular adsorbates (on HOPG electrode) at different electrode potentials (vs Ag/AgCl). Each phase map is plotted after subtracting a biexponential background. A lower phase (yellow/bright color) roughly corresponds to a higher force. Scale bars: 1 nm for x, and 0.5 nm for z. (**b**) Histograms showing the vertical distance between the first two solvation layers (d_{12}) at each potential.

Building upon the existing progress in EC-AFM and 3D-AFM, our lab achieved EC-3D-AFM in 2020 (Figure 1c).[55] We combined photothermal excitation and 3D scanning with a three-electrode EC cell that is sealed in controlled gas environment and is capable of liquid perfusion. We typically add 100–150 μL electrolyte into the cell, reaching a liquid thickness around 2 mm. Such design enables full electrochemical control in operando conditions, while avoiding extra mechanical noise during scanning by decoupling the liquid cup from the overall EC cell chamber.[55] Since the cell is fully sealed, we have been able to continuously image the same electrode-electrolyte interfaces over at least 2–3 days without observing any noticeable liquid evaporation, even for the volatile organic solvents typically used in LIBs. We have used this setup to image the EDL structure of ionic liquids and water-in-salt electrolytes on highly oriented pyrolytic graphite (HOPG) and MoS_2 electrodes, and observed their potential-dependent reconfiguration.[55–57] As a demonstration of the capability of our EC-3D-AFM to image heterogeneous electrode-electrolyte interfaces, as typical in electrochemical reactions, Figure 2a shows x-z cross section maps of the EDL of an aqueous solution on HOPG at a series of electrode potentials. Despite careful sample preparation, heterogeneous sites with angstrom-scale roughness and nanometer-scale lateral size were observed at certain locations of the HOPG surface, likely due to the adventitious adsorption of airborne organic impurities as reported before for HOPG/water interfaces.[88,89] In this heterogeneous system, we achieved angstrom resolution of the electrode surface and EDLs, resolving both the rough surface adsorbates and the EDL density variation. Further analysis reveals that the interlayer distance of the first two solvation layers (d_{12}) remains nearly constant at ~3.4 Å regardless of the applied electrode potential (Figure 2b). This spacing is close to the intermolecular distance of bulk water, indicating that water may be the dominant species in the EDL of the measured dilute aqueous solution.

Electrochemical SHINERS Characterization

While EC-3D-AFM is powerful in simultaneously imaging both the electrode surface and EDLs, it has a key limitation—the lack of direct chemical sensitivity. This is because the measured force depends on the overall molecular density distribution of the liquid, which may contain multiple different chemical species. In our recent work, we have extended the capability of EC-3D-AFM to deconvolute charge densities in highly ionic electrolytes, by combining the force map with an electrostatic solver.[57] In another work by the Garcia lab, charge deconvolution was achieved by using charge-functionalized AFM probes.[90] However, so far both of these approaches can only work for electrolytes with high ionic strength, where charged species/clusters dominate the molecular density. For dilute solutions (e.g., < 1 M salt concentration in neutral solvent), chemical profiling by 3D-AFM has not been achieved to date.

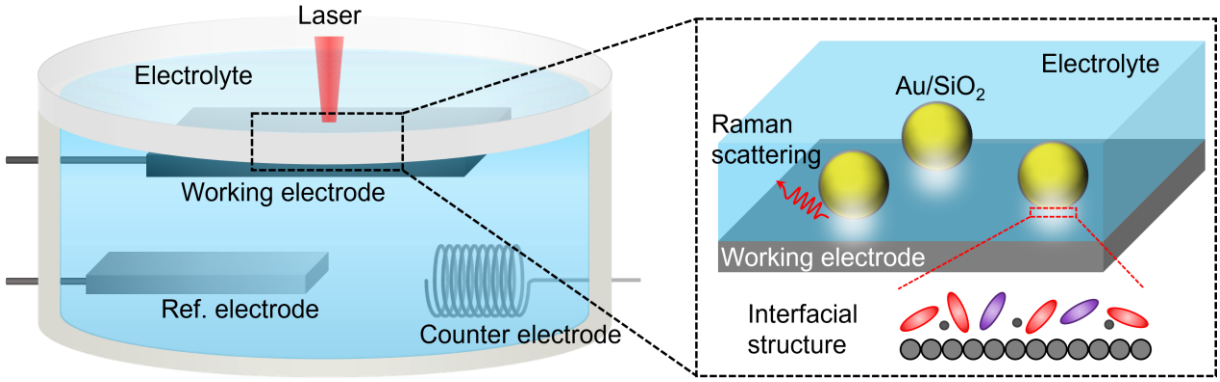

Figure 3. Schematics of the electrochemical SHINERS setup.

To overcome the limits in chemical sensitivity of EC-3D-AFM, it is desirable to combine it with complementary spectroscopy methods. However, many of the traditional surface-sensitive spectroscopy techniques, such as surface-enhanced Raman (SERS), attenuated total reflection Fourier transform infrared (ATR-FTIR), and surface-enhanced infrared absorption spectroscopy (SEIRAS), requires either plasmonic or IR-transparent substrates, thus cannot be used for graphite anode-electrolyte interfaces in LIBs. To overcome such problems, SHINERS was developed in 2010 by Li, Tian, and co-workers,[91] and has been widely used to probe electrode-electrolyte interfaces in recent years, including SEI structures.[15,46,47,92–100]

A schematic of a typical EC-SHINERS setup is shown in Figure 3. SHINERS utilizes Au/SiO_2 core/shell nanoparticles, where the core is typically 50–60 nm in diameter, and the shell is usually ~2 nm thick. When coated on a metallic electrode, the nanometer-scale gap between the particle and electrode surface is the hot spot for plasmonic and Raman enhancement, while the SiO_2 shell electronically isolates the Au core from the surrounding environment. Therefore, SHINERS is highly sensitive to the chemical species at the electrode-electrolyte interface with negligible or weak perturbation to the intrinsic EDL structure and the electrochemical activity. Since the gap-mode enhancement can be achieved for most of the highly conductive surfaces that are not too rough and not limited to plasmonic metal (Au, Ag, Cu), it can be used to probe a broad range of interfacial systems including graphite-electrolyte interfaces.[101,102]

To enable SHINERS, nanoparticle-coated area of the working electrode should be optically

accessible for the laser illumination (Figure 3). All electrodes should be physically separated but fully immersed into the electrolyte. To study battery systems, the cell is recommended to be sealed under inert argon environment to avoid the impacts of the ambient atmosphere. The overall setup can be either a three-electrode cell with a well-defined reference electrode (e.g., Li) mimicking battery half-cells, or a two-electrode cell that closely resembles a realistic battery capable of multiple charging/discharging cycling.

For battery electrolytes containing Li^+ ions, Raman spectroscopy has been used as a standard method to quantify the Li^+ solvation structure in the bulk liquid, as the solvents/anions in the Li^+ solvation shell usually have different vibrational peak positions compared to the free counterparts in solution.[30,103–105] However, although theory has predicted different Li^+ solvation structures at electrode surfaces compared to that of the bulk electrolyte,[35] experimental study of the interfacial solvation is rare. As an example, we have performed EC-SHINERS measurements of 0.71 m (molality) lithium bis(trifluoromethylsulfonyl)imide (LiTFSI) in 1-butyl-1-methylpyrrolidinium bis(trifluoromethylsulfonyl)imide (BMPy-TFSI). As shown in Figure 4, we observed strong potential-dependence of the interfacial Li^+ solvation structure. At more negative electrode potential, more Li^+ ions coordinate with $TFSI^-$ in the EDL. The deviation between interfacial and bulk Li^+ solvation structure is stronger as the electrode is more polarized. These results demonstrate the interface-sensitivity of our EC-SHINERS method, and its huge potential in unraveling the previously hidden Li^+ solvation structure in the EDLs.

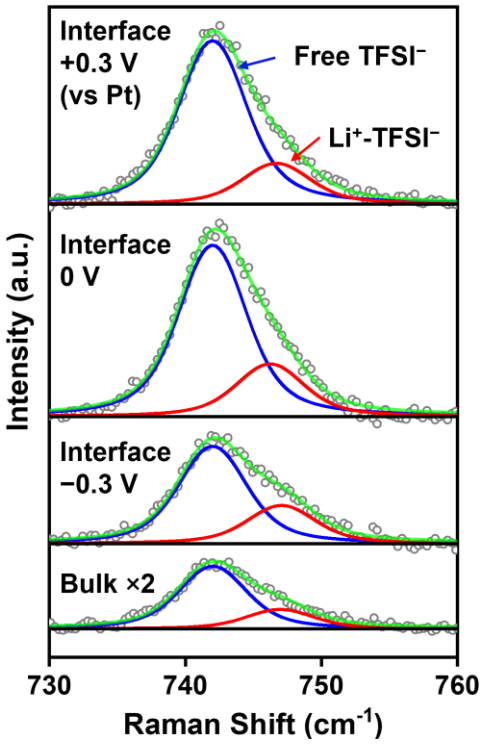

Figure 4. EC-SHINERS characterization of 0.71 m LiTFSI in BMPy-TFSI on Au(111) electrode. From top down, the extracted molar fraction of Li^+-coordinated $TFSI^-$ (vs overall $TFSI^-$) is 0.20, 0.23, 0.28, and 0.24, respectively.

Prospects for In Situ Characterization of EDL and Initial SEI Growth

Traditional LIBs have mainly relied on 1 M $LiPF_6$/carbonate systems (abbreviated as 1MEs). In recent years, the urgent demand on safer and more energy dense batteries has fostered the development of many new types of electrolytes. One of the highly promising electrolyte system is highly concentrated electrolytes (HCEs) where the amount of salts is comparable to that of solvent species.[27] Here we will discuss both 1MEs and HCEs for correlative EDL and SEI studies.

The past 1–2 decades has seen tremendous efforts on the in situ and ex situ characterization of SEIs formed in traditional 1MEs.[2,8,10–13,16–20,22] A popular hypothesis is that the SEIs contain multiple phases/compositions, with inorganic layer(s) consisting of LiF, Li_2CO_3, Li_2O, etc., and organic domain(s) composed of lithium alkyl carbonates (e.g., lithium ethylene di-carbonate, lithium ethylene mono-carbonate, and lithium methyl carbonate).[2,4–6,10,36] In HCEs, an increase in the SEI component corresponding to anion reduction is typical;[27] for example, larger amounts of LiF in the SEI is usually observed for lithium bis(fluorosulfonyl)imide (LiFSI) and LiTFSI-based HCEs, which is beneficial for enhancing the voltage and energy density of LIBs.[30,106–108] However, despite the increasingly thorough understanding of SEI composition, the dynamic SEI formation and evolution mechanism and their correlation with the EDL structure are largely unknown.

For the traditional 1MEs, we expect the Li^+ coordination number to be lower at edge sites compared to that at basal plane at negatively charged electrodes (as needed for SEI nucleation). A smaller coordination number may result in stronger polarization and thus more positive reduction potential of the coordinated solvent molecules (as one may confirm by performing density functional theory (DFT) calculations), which further leads to favorable initial electroreduction and SEI nucleation. As to the initial SEI composition, we hypothesize that it is directly linked to the chemical nature of the Li^+ solvation shell in the first EDL (number and ratio of EC vs linear carbonate), and is likely mainly organic (Figure 5a).

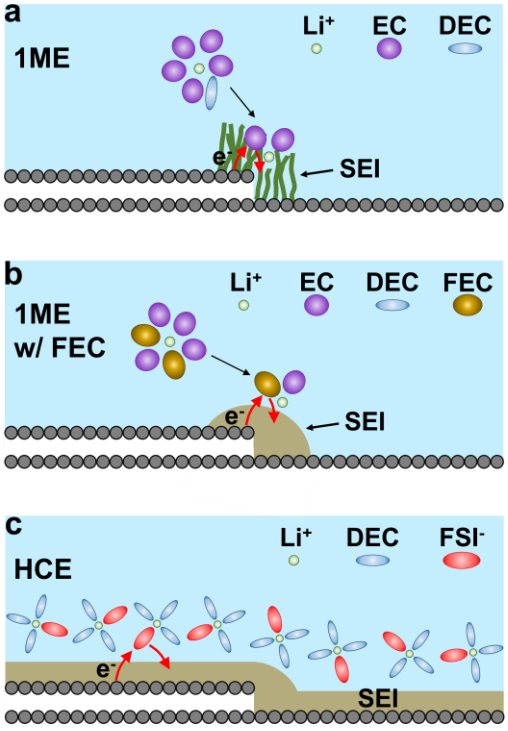

Figure 5. Hypothesized initial SEI nucleation process at graphite anode for (**a**) 1ME without additive, (**b**) 1ME with FEC additive, and (**c**) HCE.

In addition to the EC / linear carbonate solvents, commercial LIBs use various additives to improve the battery performance, among which FEC is one of the most well-known for promoting the anode stability and overall energy density of the battery.[2,22] Existing studies have revealed that FEC tends to result in higher amounts of LiF in the SEI, which is likely responsible for promoting the battery performance.[2,22,109,110] However, the dynamic SEI formation process and the spatial distribution of the LiF domains remain elusive. Previous studies on bulk electrolytes revealed that FEC competes against EC and linear carbonates to be incorporated into the Li^+ solvation shell,[109,111,112] although the solvation configuration will likely change in the charged EDL. Due to their structural similarities, we propose that FEC and EC will likely both strongly coordinate with Li^+ in the EDL; SEI nucleation may still initiate at the edge sites, although (with a sufficient amount of FEC) the composition is likely mainly inorganic and rich in LiF (Figure 5b).

In contrast to 1MEs where the Li^+ solvation shell is expected to be dominated by solvent molecules, in HCEs the salt anion species will likely strongly interact with Li^+ ions and solvent molecules forming clusters. Existing studies have shown that the SEIs formed in HCEs are significantly different from those in 1MEs, with features including higher ratio of fluoride-rich contents, less organic domains, smaller degree of SEI swelling, and better protection of graphite step sites against structural deterioration.[11,28,106,113] However, the dynamic SEI growth process in HCEs remains largely unknown. At the initial nucleation stage, key open questions are: Where does the SEI nucleation initiate (basal plane or step/edge site)? What species are reduced first forming SEI (solvent molecules or anions)? Is the initial SEI organic or inorganic? How does the EDL configuration affect the uniformity of the SEI? By combining EC-3D-AFM with EC-SHINERS characterization, these questions would be able to be resolved. For example, through continuous x-y surface imaging, EC-AFM can reveal the initial SEI nucleation sites and the uniformity of the continuously evolving SEI; by combining AFM indentation response and SHINERS peak positions, one may determine the elastic modulus and composition of SEIs; through quantification of the 3D-AFM force oscillation profiles (periodicity, correlation length, etc.), together with SHINERS peak deconvolution, one may determine the local EDL configuration.

We hypothesize that the SEI composition and onset potential likely depend not only on the ratio of Li^+-coordinated anion vs solvent species, but also the overall size of the solvation clusters and structural connectivity of the innermost EDL, due to the strong intermolecular interactions in these HCEs. For the same reason, it is likely that the electrolyte reduction is less sensitive to the local electrode structure (mimicking those of outer-sphere reactions), and we may observe SEI nucleation at both the edge and basal plane sites of graphite with similar onset potential (Figure 5c).

EDL–SEI Correlation and Predictive Design of Batteries

While the initial nucleation and growth of SEIs is critical for understanding the SEI formation mechanism, the eventual battery performance requires one or multiple charge/discharge cycles to form complete and stable SEI passivation layers.[2,22] In the battery community, tremendous amounts of efforts have been devoted to characterizing (in situ or ex situ) mature SEIs and correlating their structure with battery performance. However, to date such structure-function correlation is still largely elusive and under debate. Various features/parameters of the SEI,

including structural uniformity, ionic conductivity, elastic modulus, organic/inorganic ratio, and swelling ratio (due to electrolyte retention inside the SEI), have been proposed as possible descriptors of the battery cycling behaviors.[2,8,10–13,16–20,22] We hypothesize that, while each of these descriptors reveals a certain property of the SEI, many of them are interrelated. For example, a lower organic to inorganic domain ratio may result in lower overall porosity of the SEI, which can further lead to smaller swelling ratio and larger elastic modulus. For different applications, one may prefer to selectively enhance certain SEI characteristics. For instance, high ionic conductivity of the SEI is likely needed for fast-charging battery, while enhanced battery safety may require the SEI to be highly uniform and dense. A comprehensive investigation of the connection between SEI structure and all the battery performance metrics is beyond the scope of this perspective. Instead, we will focus on the correlation between the EDL structure and the characteristics of the mature SEI, which offers the fundamental insights needed for the predictive design of electrolytes to achieve desired SEI properties.

Through EC-3D-AFM, SHINERS, and electrochemical impedance spectroscopy measurements, as well as ex situ characterization (X-ray photoelectron spectroscopy, electron microscopy, secondary ion mass spectrometry, etc.), it will be possible to determine key SEI characteristics including the spatial uniformity, ionic conductivity, elasticity, inorganic/organic ratio, and electrolyte/solid ratio, and analyze their correlation to the EDL structure.

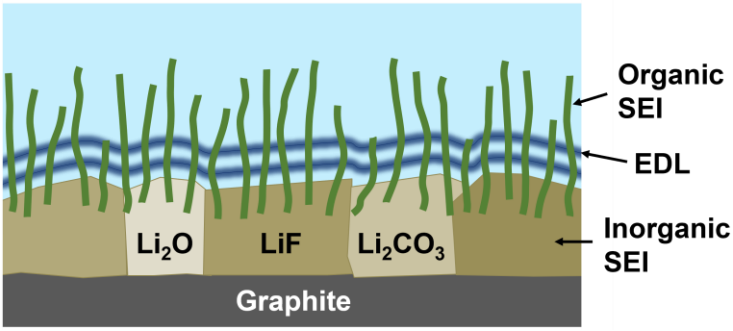

Figure 6. A hypothesized example of the general structure of a mature SEI.

Due to the sequential reduction of different electrolyte species (either Li^+-coordinated or free) at different electrode potentials, the SEIs formed in any electrolyte will likely have some degree of spatial heterogeneity (Figure 6). However, considering that the HCEs likely form interconnected nanocluster networks in the EDL with negligible amounts of uncoordinated species, while 1MEs contain mixtures of Li^+-coordinated and free species in the EDL with distinct reduction potentials, HCEs in general may favor more homogeneous SEIs than 1MEs. As to the SEI's ionic conduction properties, we hypothesize that the formation of porous organic phases may not induce observable changes to the overall SEI conductance, as the electrolytes can permeate through the pores and reach the underlying solid (either a dense, likely inorganic SEI, or the graphite electrode) (Figure 6); in contrast, the overall thickening of inorganic layers/domains (LiF, Li_2CO_3, Li_2O, etc.) may lead to a lower SEI conductance as they are likely impermeable to liquid, although the average conductivity may or may not change depending on the specific SEI structure and Li^+ ion transport mechanism. In addition, we expect the HCEs to in general produce higher inorganic/organic ratio and lower electrolyte/solid ratio in the SEIs, compared to 1MEs. Furthermore, the addition of FEC in 1MEs will likely also lead to the preferential growth of inorganic domains, especially LiF,

although the overall uniformity may be lower than those of HCEs.

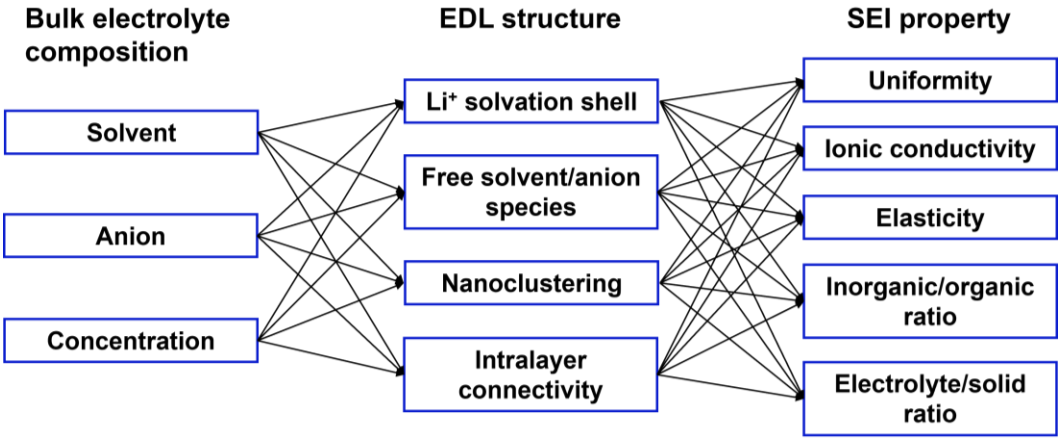

Figure 7. Schematic of the proposed intercorrelation among bulk electrolyte, EDL, and SEI.

Figure 7 summarizes the proposed thorough correlation analysis among the bulk electrolyte composition, the descriptors of EDL structure, and SEI properties. Such analysis would enable a comprehensive understanding of the effect of electrolytes on SEI growth. Further insights may be gained via DFT and molecular dynamics (MD) modeling to extract molecular descriptor parameters of the anion and solvent species (e.g., reduction potential, donor number, dipole moment, etc.). Such descriptors can be correlated with the EDL structure and SEI properties, enabling the prediction of new types of molecular electrolytes that lead to specific SEI characteristics.

As an example of predictive battery design, we hypothesize that the Coulombic efficiency (CE) of LIBs is likely strongly correlated to the inorganic/organic ratio of SEIs. SEIs with a higher inorganic/organic ratio may be overall more stable under battery cycling, resulting in a higher CE of LIBs; as an example of the various EDL-SEI correlations, the accumulation and Li^+-coordination of fluorinated species (e.g., FEC, FSI^-, and $TFSI^-$) in the EDL will likely favorably induce LiF formation, enhancing the inorganic/organic ratio, and boosting the CE of LIBs. These hypotheses can be readily tested by combining the in situ and ex situ characterization we discussed and the battery cycling tests of the graphite anode half cells and/or full LIB cells.

Outlook

Electrode-electrolyte interfaces are complex systems where heterogeneous solid and liquid species dynamically evolve, react, and restructure. This interface does not consist of just one layer of atoms. Rather, it spans over a three-dimensional volume. For battery systems, anode-electrolyte interfaces contain both the SEIs and EDLs as indispensable and interrelated structures. The impact of EDLs on SEI growth, although conceptually intuitive, has not received much attention in the battery and electrochemistry communities until very recent years. By discussing the possible mechanisms of EDL reconfiguration and SEI growth, as well as their correlations, we hope to raise the awareness that the electrode-electrolyte interfaces need to be studied holistically. Only by examining the EDLs and SEIs together, and characterizing the dynamic, holistic interfacial structure from the

very beginning to a fully mature state (complete SEI growth), can we achieve a comprehensive understanding that will be sufficient for predictive design of electrolytes for safer, more energy dense, and faster charging batteries.

Methods

EC-3D-AFM

Building upon an Asylum Cypher ES AFM with customized modifications, we conducted EC-3D-AFM measurements as outlined in our previous publications.[55–57,114] HOPG (ZYB grade, Bruker) was used as the working electrode with a platinum ring as a counter and quasi-reference electrode. Potassium sulfate (K_2SO_4, anhydrous, 99+%, analysis) was obtained from Acros Organics. To prepare a 0.1 M K_2SO_4 solution, the appropriate amount of salt was dissolved in Milli-Q water (18.2 MΩ·cm; Synergy UV system, Millipore Corporation). An FS-1500AuD AFM probe (Asylum Research) was used. The probes were cleaned with acetone, IPA and water, followed by UV Ozone. The used probe has a spring constant of 15.34 nN/nm (determined by thermal tune), a resonant frequency of 629 kHz in liquid and a quality factor of 6.2. InvOLS value was 11.26 nm/V. The EC cell was assembled according to the procedure outlined in our previous work.[55–57] The potential difference between the Pt quasi-reference and a standard Ag/AgCl reference electrode (3 M NaCl, BaSi) was measured in a separate electrochemical measurement. Before adding the electrolyte, the HOPG was mechanically exfoliated to expose a fresh surface. After the electrolyte was added, the cell was purged by argon gas for a few minutes and sealed afterwards. A Keithley 2450 SourceMeter was used to control the electrode potential. AC mode, amplitude modulation EC-3D-AFM maps were obtained with the cantilever photo-thermally excited at resonance frequency. The 3D imaging parameters were: 10 Hz z-rate, 73–85 pm free amplitude, and 29–39 pm amplitude set point.

Raman spectroscopy

LiTFSI salt (99.95%) was purchased from Sigma-Aldrich and stored in a nitrogen glove box. BMPy-TFSI (99.9%) was obtained from Iolitec and stored in an argon glove box after vacuum annealing at 105 °C for ~24 h.

We synthesized Au/SiO_2 nanoparticles, and the detail of the synthesis is provided in our previous publication.[94] The morphology of the Au/SiO_2 nanoparticles was characterized by JEOL 2100 Cryo Transmission Electron Microscope (TEM).[115–117] The nanoparticles were deposited on an Au(111) thin film grown on mica substrate (Phasis), and the nanoparticle-deposited Au film was used as the working electrode. In the EC-SHINERS experiments, we used the same electrochemical cell as EC-3D-AFM measurements with a Pt ring as the reference electrode. The electrode potential was applied using a Keithley 2450 SourceMeter. The Raman spectra acquisition was achieved by using a Raman confocal imaging system (Horiba LabRAM HR 3D-capable Raman spectroscopy) with 1800 grooves/mm grating. A 633 nm wavelength laser was focused on the nanoparticle-deposited area of the working electrode using a long working distance 50× objective. An optical filter was applied to reduce the original laser power of ~35 mW to ~3.5 mW. SHINERS spectra were collected over six accumulations, with 150 seconds integration time per accumulation. Before obtaining the SHINERS spectra, an electrochemical cleaning was performed

by applying a high positive potential over a few minutes. The Voigt function with fixed shape and width as fitting constraints was applied to deconvolute the Raman peaks. The spectra were calibrated using the free $TFSI^-$ anion peak at 742 cm^{-1}.

A spectrum of bulk electrolyte was obtained on an electrolyte-covered mica substrate. The laser focus was at 400 μm above the surface of the mica. The spectrum acquisition condition was four accumulations, with 200 seconds integration time per accumulation. The bulk spectrum was calibrated in the same way as the SHINERS spectra.

Associated Content

Notes

The authors declare no competing financial interest.

Biographies

Jaehyeon Kim earned her B.S. degree in Materials Science and Engineering from the University of Wisconsin-Madison. She is currently pursuing a Ph.D. in Materials Science and Engineering at the University of Illinois Urbana-Champaign. Her research focuses on studying solid-liquid interfaces using surface-sensitive vibrational spectroscopy. She has been awarded the PPG-MRL graduate research assistantship award.

Fujia Zhao is a Ph.D. candidate in the Department of Materials Science and Engineering at the University of Illinois Urbana-Champaign. His main research project is on combining advanced Raman spectroscopy and atomic force microscopy to study electrode-water interfaces.

Lalith Krishna Samanth Bonagiri is a Ph.D. candidate in the Department of Mechanical Science and Engineering at the University of Illinois Urbana-Champaign. His current research focuses on utilizing atomic force microscopy (AFM) to image electrode-electrolyte interfaces, with a particular emphasis on highly concentrated electrolyte systems. Additionally, he is interested in enhancing AFM imaging resolution through machine learning-based algorithms. Lalith has been honored with the TechnipFMC Educational Fund Fellowship in recognition of his outstanding academic and research achievements.

Qian Ai earned his bachelor's degree in Materials Science and Engineering from Southern University of Science and Technology in 2021. He is currently a Ph.D. student in the Department of Materials Science and Engineering at University of Illinois Urbana-Champaign. His research is focused on detecting and understanding the interfacial liquid layer structure for renewable energy systems.

Yingjie Zhang is an assistant professor at the University of Illinois Urbana-Champaign. His research focuses on in situ characterization of solid-liquid interfaces, electrocatalysis, and chemical imaging of biological cells.

Acknowledgments

We acknowledge support from the National Science Foundation under Grant No. 2339175. The experiments were performed in part in the Carl R. Woese Institute for Genomic Biology, the Materials Research Laboratory, and the Beckman Institute for Advanced Science and Technology at the University of Illinois.

References

(1) Stamenkovic, V. R.; Strmcnik, D.; Lopes, P. P.; Markovic, N. M. Energy and Fuels from Electrochemical Interfaces. *Nat. Mater.* **2017**, *16*, 57–69.

(2) Xu, K. Electrolytes and Interphases in Li-Ion Batteries and Beyond. *Chem. Rev.* **2014**, *114*, 11503–11618.

(3) Winter, M. The Solid Electrolyte Interphase – The Most Important and the Least Understood Solid Electrolyte in Rechargeable Li Batteries. *Z. Phys. Chem.* **2009**, *223*, 1395–1406.

(4) Wang, L.; Menakath, A.; Han, F.; Wang, Y.; Zavalij, P. Y.; Gaskell, K. J.; Borodin, O.; Iuga, D.; Brown, S. P.; Wang, C.; et al. Identifying the Components of the Solid–Electrolyte Interphase in Li-Ion Batteries. *Nat. Chem.* **2019**, *11*, 789–796.

(5) Wang, A.; Kadam, S.; Li, H.; Shi, S.; Qi, Y. Review on Modeling of the Anode Solid Electrolyte Interphase (SEI) for Lithium-Ion Batteries. *npj Comput. Mater.* **2018**, *4*, 15.

(6) Zhou, Y.; Su, M.; Yu, X.; Zhang, Y.; Wang, J.-G.; Ren, X.; Cao, R.; Xu, W.; Baer, D. R.; Du, Y.; et al. Real-Time Mass Spectrometric Characterization of the Solid–Electrolyte Interphase of a Lithium-Ion Battery. *Nat. Nanotechnol.* **2020**, *15*, 224–230.

(7) Yan, C.; Jiang, L.-L.; Yao, Y.-X.; Lu, Y.; Huang, J.-Q.; Zhang, Q. Nucleation and Growth Mechanism of Anion-Derived Solid Electrolyte Interphase in Rechargeable Batteries. *Angew. Chemie Int. Ed.* **2021**, *60*, 8521–8525.

(8) Zampardi, G.; Klink, S.; Kuznetsov, V.; Erichsen, T.; Maljusch, A.; La Mantia, F.; Schuhmann, W.; Ventosa, E. Combined AFM/SECM Investigation of the Solid Electrolyte Interphase in Li-Ion Batteries. *ChemElectroChem* **2015**, *2*, 1607–1611.

(9) Cresce, A. v.; Russell, S. M.; Baker, D. R.; Gaskell, K. J.; Xu, K. In Situ and Quantitative Characterization of Solid Electrolyte Interphases. *Nano Lett.* **2014**, *14*, 1405–1412.

(10) Liu, T.; Lin, L.; Bi, X.; Tian, L.; Yang, K.; Liu, J.; Li, M.; Chen, Z.; Lu, J.; Amine, K.; et al. In Situ Quantification of Interphasial Chemistry in Li-Ion Battery. *Nat. Nanotechnol.* **2019**, *14*, 50–56.

(11) Zhang, Z.; Li, Y.; Xu, R.; Zhou, W.; Li, Y.; Oyakhire, S. T.; Wu, Y.; Xu, J.; Wang, H.; Yu, Z.; et al. Capturing the Swelling of Solid-Electrolyte Interphase in Lithium Metal Batteries. *Science* **2022**, *375*, 66–70.

(12) Han, B.; Zou, Y.; Xu, G.; Hu, S.; Kang, Y.; Qian, Y.; Wu, J.; Ma, X.; Yao, J.; Li, T.; et al. Additive Stabilization of SEI on Graphite Observed Using Cryo-Electron Microscopy. *Energy Environ. Sci.* **2021**, *14*, 4882–4889.

(13) Huang, W.; Attia, P. M.; Wang, H.; Renfrew, S. E.; Jin, N.; Das, S.; Zhang, Z.; Boyle, D. T.; Li, Y.; Bazant, M. Z.; et al. Evolution of the Solid–Electrolyte Interphase on Carbonaceous Anodes Visualized by Atomic-Resolution Cryogenic Electron Microscopy. *Nano Lett.* **2019**, *19*, 5140–5148.

(14) Li, Y.; Li, Y.; Pei, A.; Yan, K.; Sun, Y.; Wu, C.-L.; Joubert, L.-M.; Chin, R.; Koh, A. L.; Yu, Y.; et al. Atomic Structure of Sensitive Battery Materials and Interfaces Revealed by Cryo–Electron Microscopy. *Science* **2017**, *358*, 506–510.

(15) Gu, Y.; You, E.-M.; Lin, J.-D.; Wang, J.-H.; Luo, S.-H.; Zhou, R.-Y.; Zhang, C.-J.; Yao, J.-L.; Li, H.-Y.; Li, G.; et al. Resolving Nanostructure and Chemistry of Solid-Electrolyte Interphase on Lithium Anodes by Depth-Sensitive Plasmon-Enhanced Raman Spectroscopy. *Nat. Commun.* **2023**, *14*, 3536.

(16) Piernas-Muñoz, M. J.; Tornheim, A.; Trask, S.; Zhang, Z.; Bloom, I. Surface-Enhanced Raman Spectroscopy (SERS): A Powerful Technique to Study the SEI Layer in Batteries. *Chem. Commun.* **2021**, *57*, 2253–2256.

(17) Amaral, M. M.; Real, C. G.; Yukuhiro, V. Y.; Doubek, G.; Fernandez, P. S.; Singh, G.; Zanin, H. In Situ and Operando Infrared Spectroscopy of Battery Systems: Progress and Opportunities. *J. Energy Chem.* **2023**, *81*, 472–491.

(18) Wood, K. N.; Teeter, G. XPS on Li-Battery-Related Compounds: Analysis of Inorganic SEI Phases and a Methodology for Charge Correction. *ACS Appl. Energy Mater.* **2018**, *1*, 4493–4504.

(19) Chattopadhyay, S.; Lipson, A. L.; Karmel, H. J.; Emery, J. D.; Fister, T. T.; Fenter, P. A.; Hersam, M. C.; Bedzyk, M. J. In Situ X-Ray Study of the Solid Electrolyte Interphase (SEI) Formation on Graphene as a Model Li-Ion Battery Anode. *Chem. Mater.* **2012**, *24*, 3038–3043.

(20) Steinhauer, M.; Stich, M.; Kurniawan, M.; Seidlhofer, B.-K.; Trapp, M.; Bund, A.; Wagner, N.; Friedrich, K. A. In Situ Studies of Solid Electrolyte Interphase (SEI) Formation on Crystalline Carbon Surfaces by Neutron Reflectometry and Atomic Force Microscopy. *ACS Appl. Mater. Interfaces* **2017**, *9*, 35794–35801.

(21) Kawaura, H.; Harada, M.; Kondo, Y.; Mizutani, M.; Takahashi, N.; Yamada, N. L. Effects of Lithium Bis(Oxalate)Borate Electrolyte Additive on the Formation of a Solid Electrolyte Interphase on Amorphous Carbon Electrodes by Operando Time-Slicing Neutron Reflectometry. *ACS Appl. Mater. Interfaces* **2022**, *14*, 24526–24535.

(22) Xu, K. Nonaqueous Liquid Electrolytes for Lithium-Based Rechargeable Batteries. *Chem. Rev.* **2004**, *104*, 4303–4418.

(23) Zhao, W.; Ji, Y.; Zhang, Z.; Lin, M.; Wu, Z.; Zheng, X.; Li, Q.; Yang, Y. Recent Advances in the Research of Functional Electrolyte Additives for Lithium-Ion Batteries. *Curr. Opin. Electrochem.* **2017**, *6*, 84–91.

(24) Tang, X.; Lv, S.; Jiang, K.; Zhou, G.; Liu, X. Recent Development of Ionic Liquid-Based Electrolytes in Lithium-Ion Batteries. *J. Power Sources* **2022**, *542*, 231792.

(25) Wang, Y.; Yi, J.; Xia, Y. Recent Progress in Aqueous Lithium-Ion Batteries. *Adv. Energy*

Mater. **2012**, *2*, 830–840.

(26) Suo, L.; Borodin, O.; Gao, T.; Olguin, M.; Ho, J.; Fan, X.; Luo, C.; Wang, C.; Xu, K. "Water-in-Salt" Electrolyte Enables High-Voltage Aqueous Lithium-Ion Chemistries. *Science* **2015**, *350*, 938–943.

(27) Yamada, Y.; Wang, J.; Ko, S.; Watanabe, E.; Yamada, A. Advances and Issues in Developing Salt-Concentrated Battery Electrolytes. *Nat. Energy* **2019**, *4*, 269–280.

(28) Liu, X.-R.; Wang, L.; Wan, L.-J.; Wang, D. In Situ Observation of Electrolyte-Concentration-Dependent Solid Electrolyte Interphase on Graphite in Dimethyl Sulfoxide. *ACS Appl. Mater. Interfaces* **2015**, *7*, 9573–9580.

(29) Sodeyama, K.; Yamada, Y.; Aikawa, K.; Yamada, A.; Tateyama, Y. Sacrificial Anion Reduction Mechanism for Electrochemical Stability Improvement in Highly Concentrated Li-Salt Electrolyte. *J. Phys. Chem. C* **2014**, *118*, 14091–14097.

(30) Yamada, Y.; Furukawa, K.; Sodeyama, K.; Kikuchi, K.; Yaegashi, M.; Tateyama, Y.; Yamada, A. Unusual Stability of Acetonitrile-Based Superconcentrated Electrolytes for Fast-Charging Lithium-Ion Batteries. *J. Am. Chem. Soc.* **2014**, *136*, 5039–5046.

(31) Xu, K. "Charge-Transfer" Process at Graphite/Electrolyte Interface and the Solvation Sheath Structure of Li^+ in Nonaqueous Electrolytes. *J. Electrochem. Soc.* **2007**, *154*, A162.

(32) von Wald Cresce, A.; Borodin, O.; Xu, K. Correlating Li^+ Solvation Sheath Structure with Interphasial Chemistry on Graphite. *J. Phys. Chem. C* **2012**, *116*, 26111–26117.

(33) Sun, S.; Kim, G.; Lee, D.; Park, E.; Myeong, S.; Son, B.; Lee, K.; Jang, M.; Paik, U.; Song, T. Modulating SEI Formation via Tuning the Solvation Sheath for Lithium Metal Batteries. *Chem. Commun.* **2022**, *58*, 9834–9837.

(34) Kim, S. C.; Kong, X.; Vilá, R. A.; Huang, W.; Chen, Y.; Boyle, D. T.; Yu, Z.; Wang, H.; Bao, Z.; Qin, J.; et al. Potentiometric Measurement to Probe Solvation Energy and Its Correlation to Lithium Battery Cyclability. *J. Am. Chem. Soc.* **2021**, *143*, 10301–10308.

(35) Wu, Q.; McDowell, M. T.; Qi, Y. Effect of the Electric Double Layer (EDL) in Multicomponent Electrolyte Reduction and Solid Electrolyte Interphase (SEI) Formation in Lithium Batteries. *J. Am. Chem. Soc.* **2023**, *145*, 2473–2484.

(36) Chen, Y.; Wu, W.; Gonzalez-Munoz, S.; Forcieri, L.; Wells, C.; Jarvis, S. P.; Wu, F.; Young, R.; Dey, A.; Isaacs, M.; et al. Nanoarchitecture Factors of Solid Electrolyte Interphase Formation via 3D Nano-Rheology Microscopy and Surface Force-Distance Spectroscopy. *Nat. Commun.* **2023**, *14*, 1321.

(37) Borodin, O.; Ren, X.; Vatamanu, J.; von Wald Cresce, A.; Knap, J.; Xu, K. Modeling Insight into Battery Electrolyte Electrochemical Stability and Interfacial Structure. *Acc. Chem. Res.* **2017**, *50*, 2886–2894.

(38) Yan, C.; Li, H.-R.; Chen, X.; Zhang, X.-Q.; Cheng, X.-B.; Xu, R.; Huang, J.-Q.; Zhang, Q. Regulating the Inner Helmholtz Plane for Stable Solid Electrolyte Interphase on Lithium Metal Anodes. *J. Am. Chem. Soc.* **2019**, *141*, 9422–9429.

(39) Kumeda, T.; Tajiri, H.; Sakata, O.; Hoshi, N.; Nakamura, M. Effect of Hydrophobic Cations on the Oxygen Reduction Reaction on Single–crystal Platinum Electrodes. *Nat. Commun.* **2018**, *9*, 4378.

(40) Kondo, T.; Masuda, T.; Aoki, N.; Uosaki, K. Potential-Dependent Structures and Potential-Induced Structure Changes at Pt(111) Single-Crystal Electrode/Sulfuric and Perchloric Acid Interfaces in the Potential Region between Hydrogen Underpotential Deposition and Surface Oxide Formation by In Situ Surface X-ray Scattering. *J. Phys. Chem. C* **2016**, *120*, 16118–16131.

(41) Velasco-Velez, J.-J.; Wu, C. H.; Pascal, T. A.; Wan, L. F.; Guo, J.; Prendergast, D.; Salmeron, M. The Structure of Interfacial Water on Gold Electrodes Studied by X-Ray Absorption Spectroscopy. *Science* **2014**, *346*, 831–834.

(42) Braunschweig, B.; Mukherjee, P.; Haan, J. L.; Dlott, D. D. Vibrational Sum-Frequency Generation Study of the CO_2 Electrochemical Reduction at Pt/EMIM-BF_4 Solid/Liquid Interfaces. *J. Electroanal. Chem.* **2017**, *800*, 144–150.

(43) Raberg, J. H.; Vatamanu, J.; Harris, S. J.; van Oversteeg, C. H. M.; Ramos, A.; Borodin, O.; Cuk, T. Probing Electric Double-Layer Composition via in Situ Vibrational Spectroscopy and Molecular Simulations. *J. Phys. Chem. Lett.* **2019**, *10*, 3381–3389.

(44) Li, J.; Li, X.; Gunathunge, C. M.; Waegele, M. M. Hydrogen Bonding Steers the Product Selectivity of Electrocatalytic CO Reduction. *Proc. Natl. Acad. Sci.* **2019**, *116*, 9220–9229.

(45) Liljeblad, J. F. D.; Tyrode, E. Vibrational Sum Frequency Spectroscopy Studies at Solid/Liquid Interfaces: Influence of the Experimental Geometry in the Spectral Shape and Enhancement. *J. Phys. Chem. C* **2012**, *116*, 22893–22903.

(46) Li, C.-Y.; Le, J.-B.; Wang, Y.-H.; Chen, S.; Yang, Z.-L.; Li, J.-F.; Cheng, J.; Tian, Z.-Q. In Situ Probing Electrified Interfacial Water Structures at Atomically Flat Surfaces. *Nat. Mater.* **2019**, *18*, 697–701.

(47) Wang, Y.-H.; Zheng, S.; Yang, W.-M.; Zhou, R.-Y.; He, Q.-F.; Radjenovic, P.; Dong, J.-C.; Li, S.; Zheng, J.; Yang, Z.-L.; et al. In Situ Raman Spectroscopy Reveals the Structure and Dissociation of Interfacial Water. *Nature* **2021**, *600*, 81–85.

(48) Fukuma, T.; Ueda, Y.; Yoshioka, S.; Asakawa, H. Atomic-Scale Distribution of Water Molecules at the Mica-Water Interface Visualized by Three-Dimensional Scanning Force Microscopy. *Phys. Rev. Lett.* **2010**, *104*, 016101.

(49) Umeda, K.; Zivanovic, L.; Kobayashi, K.; Ritala, J.; Kominami, H.; Spijker, P.; Foster, A. S.; Yamada, H. Atomic-Resolution Three-Dimensional Hydration Structures on a Heterogeneously Charged Surface. *Nat. Commun.* **2017**, *8*, 2111.

(50) Umeda, K.; Kobayashi, K.; Minato, T.; Yamada, H. Atomic-Scale 3D Local Hydration Structures Influenced by Water-Restricting Dimensions. *Langmuir* **2018**, *34*, 9114–9121.

(51) Umeda, K.; Kobayashi, K.; Minato, T.; Yamada, H. Atomic-Level Viscosity Distribution in the Hydration Layer. *Phys. Rev. Lett.* **2019**, *122*, 116001.

(52) Martin-Jimenez, D.; Chacon, E.; Tarazona, P.; Garcia, R. Atomically Resolved Three-

Dimensional Structures of Electrolyte Aqueous Solutions near a Solid Surface. *Nat. Commun.* **2016**, *7*, 12164.

(53) Martin-Jimenez, D.; Garcia, R. Identification of Single Adsorbed Cations on Mica–Liquid Interfaces by 3D Force Microscopy. *J. Phys. Chem. Lett.* **2017**, *8*, 5707–5711.

(54) Uhlig, M. R.; Martin-Jimenez, D.; Garcia, R. Atomic-Scale Mapping of Hydrophobic Layers on Graphene and Few-Layer MoS_2 and WSe_2 in Water. *Nat. Commun.* **2019**, *10*, 2606.

(55) Zhou, S.; Panse, K. S.; Motevaselian, M. H.; Aluru, N. R.; Zhang, Y. Three-Dimensional Molecular Mapping of Ionic Liquids at Electrified Interfaces. *ACS Nano* **2020**, *14*, 17515–17523.

(56) Panse, K. S.; Wu, H.; Zhou, S.; Zhao, F.; Aluru, N. R.; Zhang, Y. Innermost Ion Association Configuration Is a Key Structural Descriptor of Ionic Liquids at Electrified Interfaces. *J. Phys. Chem. Lett.* **2022**, *13*, 9464–9472.

(57) Bonagiri, L. K. S.; Panse, K. S.; Zhou, S.; Wu, H.; Aluru, N. R.; Zhang, Y. Real-Space Charge Density Profiling of Electrode–Electrolyte Interfaces with Angstrom Depth Resolution. *ACS Nano* **2022**, *16*, 19594–19604.

(58) Chen, C. H.; Vesecky, S. M.; Gewirth, A. A. In Situ Atomic Force Microscopy of Underpotential Deposition of Silver on Gold(111). *J. Am. Chem. Soc.* **1992**, *114*, 451–458.

(59) Macpherson, J. V; Unwin, P. R.; Hillier, A. C.; Bard, A. J. In-Situ Imaging of Ionic Crystal Dissolution Using an Integrated Electrochemical/AFM Probe. *J. Am. Chem. Soc.* **1996**, *118*, 6445–6452.

(60) Manne, S.; Hansma, P. K.; Massie, J.; Elings, V. B.; Gewirth, A. A. Atomic-Resolution Electrochemistry with the Atomic Force Microscope: Copper Deposition on Gold. *Science* **1991**, *251*, 183–186.

(61) Hillier, A. C.; Ward, M. D. Atomic Force Microscopy of the Electrochemical Nucleation and Growth of Molecular Crystals. *Science* **1994**, *263*, 1261–1264.

(62) Pérez, R.; Štich, I.; Payne, M. C.; Terakura, K. Surface-Tip Interactions in Noncontact Atomic-Force Microscopy on Reactive Surfaces: Si(111). *Phys. Rev. B* **1998**, *58*, 10835–10849.

(63) Erlandsson, R.; Olsson, L.; Mårtensson, P. Inequivalent Atoms and Imaging Mechanisms in AC-Mode Atomic-Force Microscopy of Si(111)7×7. *Phys. Rev. B* **1996**, *54*, R8309–R8312.

(64) Quate, C. F. The AFM as a Tool for Surface Imaging. *Surf. Sci.* **1994**, *299–300*, 980–995.

(65) Shiraishi, S.; Kanamura, K.; Takehara, Z. Imaging for Uniformity of Lithium Metal Surface Using Tapping Mode-Atomic Force and Surface Potential Microscopy. *J. Phys. Chem. B* **2001**, *105*, 123–134.

(66) Kueng, A.; Kranz, C.; Mizaikoff, B.; Lugstein, A.; Bertagnolli, E. Combined Scanning Electrochemical Atomic Force Microscopy for Tapping Mode Imaging. *Appl. Phys. Lett.*

2003, *82*, 1592–1594.

(67) Stieg, A. Z.; Rasool, H. I.; Gimzewski, J. K. A Flexible, Highly Stable Electrochemical Scanning Probe Microscope for Nanoscale Studies at the Solid-Liquid Interface. *Rev. Sci. Instrum.* **2008**, *79*, 103701.

(68) Boussaad, S.; Tao, N. J. Electron Transfer and Adsorption of Myoglobin on Self-Assembled Surfactant Films: An Electrochemical Tapping-Mode AFM Study. *J. Am. Chem. Soc.* **1999**, *121*, 4510–4515.

(69) Shiraishi, S.; Kanamura, K. The Observation of Electrochemical Dissolution of Lithium Metal Using Electrochemical Quartz Crystal Microbalance and In-Situ Tapping Mode Atomic Force Microscopy. *Langmuir* **1998**, *14*, 7082–7086.

(70) Martin, Y.; Williams, C. C.; Wickramasinghe, H. K. Atomic Force Microscope–Force Mapping and Profiling on a Sub 100-Å Scale. *J. Appl. Phys.* **1987**, *61*, 4723–4729.

(71) Carrasco, C.; Ares, P.; de Pablo, P. J.; Gómez-Herrero, J. Cutting down the Forest of Peaks in Acoustic Dynamic Atomic Force Microscopy in Liquid. *Rev. Sci. Instrum.* **2008**, *79*, 126106.

(72) Fukuma, T.; Kimura, M.; Kobayashi, K.; Matsushige, K.; Yamada, H. Development of Low Noise Cantilever Deflection Sensor for Multienvironment Frequency-Modulation Atomic Force Microscopy. *Rev. Sci. Instrum.* **2005**, *76*, 53704.

(73) Labuda, A.; Kobayashi, K.; Kiracofe, D.; Suzuki, K.; Grütter, P. H.; Yamada, H. Comparison of Photothermal and Piezoacoustic Excitation Methods for Frequency and Phase Modulation Atomic Force Microscopy in Liquid Environments. *AIP Adv.* **2011**, *1*, 22136.

(74) Xu, K.; Sun, W.; Shao, Y.; Wei, F.; Zhang, X.; Wang, W.; Li, P. Recent Development of PeakForce Tapping Mode Atomic Force Microscopy and Its Applications on Nanoscience. *Nanotechnol. Rev.* **2018**, *7*, 605–621.

(75) Wang, W.-W.; Gu, Y.; Wang, J.-H.; Chen, Z.-B.; Yin, X.-T.; Wu, Q.-H.; Yan, J.-W.; Mao, B.-W. Probing Mechanical Properties of Solid-Electrolyte Interphases on Li Nuclei by In Situ AFM. *J. Electrochem. Soc.* **2022**, *169*, 20563.

(76) Shen, C.; Wang, S.; Jin, Y.; Han, W.-Q. In Situ AFM Imaging of Solid Electrolyte Interfaces on HOPG with Ethylene Carbonate and Fluoroethylene Carbonate-Based Electrolytes. *ACS Appl. Mater. Interfaces* **2015**, *7*, 25441–25447.

(77) Wan, J.; Hao, Y.; Shi, Y.; Song, Y.-X.; Yan, H.-J.; Zheng, J.; Wen, R.; Wan, L.-J. Ultra-Thin Solid Electrolyte Interphase Evolution and Wrinkling Processes in Molybdenum Disulfide-Based Lithium-Ion Batteries. *Nat. Commun.* **2019**, *10*, 3265.

(78) Wolff, B.; Hausen, F. Mechanical Evolution of Solid Electrolyte Interphase on Metallic Lithium Studied by in Situ Atomic Force Microscopy. *J. Electrochem. Soc.* **2023**, *170*, 10534.

(79) Ramos, D.; Tamayo, J.; Mertens, J.; Calleja, M. Photothermal Excitation of Microcantilevers in Liquids. *J. Appl. Phys.* **2006**, *99*, 124904.

(80) Nishida, S.; Kobayashi, D.; Sakurada, T.; Nakazawa, T.; Hoshi, Y.; Kawakatsu, H. Photothermal Excitation and Laser Doppler Velocimetry of Higher Cantilever Vibration Modes for Dynamic Atomic Force Microscopy in Liquid. *Rev. Sci. Instrum.* **2008**, *79*, 123703.

(81) Fukuma, T. Wideband Low-Noise Optical Beam Deflection Sensor with Photothermal Excitation for Liquid-Environment Atomic Force Microscopy. *Rev. Sci. Instrum.* **2009**, *80*, 23707.

(82) Adam, H.; Rode, S.; Schreiber, M.; Kobayashi, K.; Yamada, H.; Kühnle, A. Photothermal Excitation Setup for a Modified Commercial Atomic Force Microscope. *Rev. Sci. Instrum.* **2014**, *85*, 23703.

(83) Yamashita, H.; Kodera, N.; Miyagi, A.; Uchihashi, T.; Yamamoto, D.; Ando, T. Tip-Sample Distance Control Using Photothermal Actuation of a Small Cantilever for High-Speed Atomic Force Microscopy. *Rev. Sci. Instrum.* **2007**, *78*, 83702.

(84) Miyazawa, K.; Kobayashi, N.; Watkins, M.; Shluger, A. L.; Amano, K.; Fukuma, T. A Relationship between Three-Dimensional Surface Hydration Structures and Force Distribution Measured by Atomic Force Microscopy. *Nanoscale* **2016**, *8*, 7334–7342.

(85) Yurtsever, A.; Wang, P.-X.; Priante, F.; Morais Jaques, Y.; Miyazawa, K.; MacLachlan, M. J.; Foster, A. S.; Fukuma, T. Molecular Insights on the Crystalline Cellulose-Water Interfaces via Three-Dimensional Atomic Force Microscopy. *Sci. Adv.* **2024**, *8*, eabq0160.

(86) Söngen, H.; Reischl, B.; Miyata, K.; Bechstein, R.; Raiteri, P.; Rohl, A. L.; Gale, J. D.; Fukuma, T.; Kühnle, A. Resolving Point Defects in the Hydration Structure of Calcite (10.4) with Three-Dimensional Atomic Force Microscopy. *Phys. Rev. Lett.* **2018**, *120*, 116101.

(87) Arvelo, D. M.; Uhlig, M. R.; Comer, J.; García, R. Interfacial Layering of Hydrocarbons on Pristine Graphite Surfaces Immersed in Water. *Nanoscale* **2022**, *14*, 14178–14184.

(88) Nioradze, N.; Chen, R.; Kurapati, N.; Khvataeva-Domanov, A.; Mabic, S.; Amemiya, S. Organic Contamination of Highly Oriented Pyrolytic Graphite As Studied by Scanning Electrochemical Microscopy. *Anal. Chem.* **2015**, *87*, 4836–4843.

(89) Garcia, R. Interfacial Liquid Water on Graphite, Graphene, and 2D Materials. *ACS Nano* **2023**, *17*, 51–69.

(90) Benaglia, S.; Uhlig, M. R.; Hernández-Muñoz, J.; Chacón, E.; Tarazona, P.; Garcia, R. Tip Charge Dependence of Three-Dimensional AFM Mapping of Concentrated Ionic Solutions. *Phys. Rev. Lett.* **2021**, *127*, 196101.

(91) Li, J. F.; Huang, Y. F.; Ding, Y.; Yang, Z. L.; Li, S. B.; Zhou, X. S.; Fan, F. R.; Zhang, W.; Zhou, Z. Y.; Wu, D. Y.; et al. Shell-Isolated Nanoparticle-Enhanced Raman Spectroscopy. *Nature* **2010**, *464*, 392–395.

(92) Gu, Y.; Tang, S.; Yi, J.; Luo, S.-H.; Li, C.-Y.; Liu, G.; Yan, J.; Li, J.-F.; Mao, B.-W.; Tian, Z.-Q. Nanostructure-Based Plasmon-Enhanced Raman Spectroscopic Strategies for Characterization of the Solid–Electrolyte Interphase: Opportunities and Challenges. *J. Phys. Chem. C* **2023**, *127*, 13466–13477.

(93) Li, C.-Y.; Chen, M.; Liu, S.; Lu, X.; Meng, J.; Yan, J.; Abruña, H. D.; Feng, G.; Lian, T. Unconventional Interfacial Water Structure of Highly Concentrated Aqueous Electrolytes at Negative Electrode Polarizations. *Nat. Commun.* **2022**, *13*, 5330.

(94) Kim, J.; Zhao, F.; Zhou, S.; Panse, K. S.; Zhang, Y. Spectroscopic Investigation of the Structure of a Pyrrolidinium-Based Ionic Liquid at Electrified Interfaces. *J. Chem. Phys.* **2022**, *156*, 114701.

(95) Zhang, M.; Yu, L.-J.; Huang, Y.-F.; Yan, J.-W.; Liu, G.-K.; Wu, D.-Y.; Tian, Z.-Q.; Mao, B.-W. Extending the Shell-Isolated Nanoparticle-Enhanced Raman Spectroscopy Approach to Interfacial Ionic Liquids at Single Crystal Electrode Surfaces. *Chem. Commun.* **2014**, *50*, 14740–14743.

(96) Dong, J. C.; Zhang, X. G.; Briega-Martos, V.; Jin, X.; Yang, J.; Chen, S.; Yang, Z. L.; Wu, D. Y.; Feliu, J. M.; Williams, C. T.; et al. In Situ Raman Spectroscopic Evidence for Oxygen Reduction Reaction Intermediates at Platinum Single-Crystal Surfaces. *Nat. Energy* **2019**, *4*, 60–67.

(97) Huang, Y.-F.; Kooyman, P. J.; Koper, M. T. M. Intermediate Stages of Electrochemical Oxidation of Single-Crystalline Platinum Revealed by in Situ Raman Spectroscopy. *Nat. Commun.* **2016**, *7*, 12440.

(98) Fernández-Vidal, J.; Koper, M. T. M. Effect of a Physisorbed Tetrabutylammonium Cation Film on Alkaline Hydrogen Evolution Reaction on Pt Single-Crystal Electrodes. *ACS Catal.* **2024**, *14*, 8130–8137.

(99) Martín-Yerga, D.; Milan, D. C.; Xu, X.; Fernández-Vidal, J.; Whalley, L.; Cowan, A. J.; Hardwick, L. J.; Unwin, P. R. Dynamics of Solid-Electrolyte Interphase Formation on Silicon Electrodes Revealed by Combinatorial Electrochemical Screening. *Angew. Chemie Int. Ed.* **2022**, *61*, e202207184.

(100) Wang, Y.-H.; Li, S.; Zhou, R.-Y.; Zheng, S.; Zhang, Y.-J.; Dong, J.-C.; Yang, Z.-L.; Pan, F.; Tian, Z.-Q.; Li, J.-F. In Situ Electrochemical Raman Spectroscopy and Ab Initio Molecular Dynamics Study of Interfacial Water on a Single-Crystal Surface. *Nat. Protoc.* **2023**, *18*, 883–901.

(101) Ikeda, K.; Sato, J.; Fujimoto, N.; Hayazawa, N.; Kawata, S.; Uosaki, K. Plasmonic Enhancement of Raman Scattering on Non-SERS-Active Platinum Substrates. *J. Phys. Chem. C* **2009**, *113*, 11816–11821.

(102) Sun, A. Y.; Lee, Y.-C.; Chang, S.-W.; Chen, S.-L.; Wang, H.-C.; Wan, D.; Chen, H.-L. Diverse Substrate-Mediated Local Electric Field Enhancement of Metal Nanoparticles for Nanogap-Enhanced Raman Scattering. *Anal. Chem.* **2021**, *93*, 4299–4307.

(103) Li, T.; Zhang, X.-Q.; Yao, N.; Yao, Y.-X.; Hou, L.-P.; Chen, X.; Zhou, M.-Y.; Huang, J.-Q.; Zhang, Q. Stable Anion-Derived Solid Electrolyte Interphase in Lithium Metal Batteries. *Angew. Chemie Int. Ed.* **2021**, *60*, 22683–22687.

(104) Su, L.; Zhao, X.; Yi, M.; Charalambous, H.; Celio, H.; Liu, Y.; Manthiram, A. Uncovering the Solvation Structure of $LiPF_6$-Based Localized Saturated Electrolytes and Their Effect on $LiNiO_2$-Based Lithium-Metal Batteries. *Adv. Energy Mater.* **2022**, *12*, 2201911.

(105) Fawdon, J.; Ihli, J.; Mantia, F. La; Pasta, M. Characterising Lithium-Ion Electrolytes via Operando Raman Microspectroscopy. *Nat. Commun.* **2021**, *12*, 4053.

(106) Fan, X.; Chen, L.; Ji, X.; Deng, T.; Hou, S.; Chen, J.; Zheng, J.; Wang, F.; Jiang, J.; Xu, K.; et al. Highly Fluorinated Interphases Enable High-Voltage Li-Metal Batteries. *Chem* **2018**, *4*, 174–185.

(107) Yamada, Y.; Usui, K.; Chiang, C. H.; Kikuchi, K.; Furukawa, K.; Yamada, A. General Observation of Lithium Intercalation into Graphite in Ethylene-Carbonate-Free Superconcentrated Electrolytes. *ACS Appl. Mater. Interfaces* **2014**, *6*, 10892–10899.

(108) Suo, L.; Xue, W.; Gobet, M.; Greenbaum, S. G.; Wang, C.; Chen, Y.; Yang, W.; Li, Y.; Li, J. Fluorine-Donating Electrolytes Enable Highly Reversible 5-V-Class Li Metal Batteries. *Proc. Natl. Acad. Sci.* **2018**, *115*, 1156–1161.

(109) Hou, T.; Yang, G.; Rajput, N. N.; Self, J.; Park, S.-W.; Nanda, J.; Persson, K. A. The Influence of FEC on the Solvation Structure and Reduction Reaction of $LiPF_6$/EC Electrolytes and Its Implication for Solid Electrolyte Interphase Formation. *Nano Energy* **2019**, *64*, 103881.

(110) Wang, Y.; Liu, Y.; Tu, Y.; Wang, Q. Reductive Decomposition of Solvents and Additives toward Solid-Electrolyte Interphase Formation in Lithium-Ion Battery. *J. Phys. Chem. C* **2020**, *124*, 9099–9108.

(111) Wang, Z.; Sun, Z.; Shi, Y.; Qi, F.; Gao, X.; Yang, H.; Cheng, H.-M.; Li, F. Ion-Dipole Chemistry Drives Rapid Evolution of Li Ions Solvation Sheath in Low-Temperature Li Batteries. *Adv. Energy Mater.* **2021**, *11*, 2100935.

(112) Piao, N.; Liu, S.; Zhang, B.; Ji, X.; Fan, X.; Wang, L.; Wang, P.-F.; Jin, T.; Liou, S.-C.; Yang, H.; et al. Lithium Metal Batteries Enabled by Synergetic Additives in Commercial Carbonate Electrolytes. *ACS Energy Lett.* **2021**, *6*, 1839–1848.

(113) Zhang, H.; Song, Z.; Fang, J.; Li, K.; Zhang, M.; Li, Z.; Yang, L.; Pan, F. Electrolyte Optimization for Graphite Anodes toward Fast Charging. *J. Phys. Chem. C* **2023**, *127*, 2755–2765.

(114) Panse, K. S.; Zhou, S.; Zhang, Y. 3D Mapping of the Structural Transitions in Wrinkled 2D Membranes: Implications for Reconfigurable Electronics, Memristors, and Bioelectronic Interfaces. *ACS Appl. Nano Mater.* **2019**, *2*, 5779–5786.

(115) Zhao, F.; Zhou, S.; Zhang, Y. Ultrasensitive Detection of Hydrogen Peroxide Using Bi_2Te_3 Electrochemical Sensors. *ACS Appl. Mater. Interfaces* **2021**, *13*, 4761–4767.

(116) Matsuura, J.; Sheelam, A.; Zhang, Y. Tandem Supported, High Metal-Loading, Non-PGM Electrocatalysts for Oxygen Reduction Reaction. *APL Energy* **2024**, *2*, 26103.

(117) Bonagiri, L. K. S.; Wang, Z.; Zhou, S.; Zhang, Y. Precise Surface Profiling at the Nanoscale Enabled by Deep Learning. *Nano Lett.* **2024**, *24*, 2589–2595.

Table of Contents Graphic